Numerical simulation of elastic buckling in 3D concrete printing using the lattice model with geometric nonlinearity

Chang, Ze; Zhang, Hongzhi; Liang, Minfei; Schlangen, Erik; Šavija, Branko

DOI
10.1016/j.autcon.2022.104485

Publication date
2022

Document Version
Final published version

Published in
Automation in Construction

Automation in Construction 142 (2022) 104485

Contents lists available at ScienceDirect

Automation in Construction

journal homepage: www.elsevier.com/locate/autcon

Numerical simulation of elastic buckling in 3D concrete printing using the lattice model with geometric nonlinearity

Ze Chang [a], Hongzhi Zhang [b], Minfei Liang [a,*], Erik Schlangen [a], Branko Šavija [a]

[a] Microlab, Faculty of Civil Engineering and Geosciences, Delft University of Technology, 2628, CN, Delft, the Netherlands
[b] School of Qilu Transportation, Shandong University, Jinan, PR China

ARTICLE INFO

Keywords:
3D concrete printing
Geometric nonlinearity
Elastic buckling
Buildability quantification

ABSTRACT

This paper explores buildability quantification of randomly meshed 3D printed concrete objects by considering structural failure by elastic buckling. The newly proposed model considers the most relevant printing parameters, including time-dependent material behaviors, printing velocity, localized damage and influence of sequential printing process. The computational uniaxial compression tests were first conducted to calibrate age-dependent elastic modulus and yield stress. Subsequently, analyses of the 3D printing process of a free wall structure and a square layout were performed. The model can reproduce the asymmetry of buckling failure accurately and the predicted critical printing height is in excellent agreement with experimental data from the literature. It can be concluded the combined effect of material variability and non-uniform gravitational loading due to sequential printing process resulted in structural failure during 3D concrete printing. Using this model, printing parameters can be optimized and a suitable printing scheme can be devised to improve structure buildability.

1. Introduction

For some decades now, additive manufacturing has been a revolutionary technology which generates enormous interest in both industrial and academic applications [1]. 3D concrete printing (3DCP), an automated construction method, is able to achieve physical realization of a computer-designed model through material deposition [2–5]. This innovative technique can considerably accelerate the construction process, and make it economically and technically feasible to implement complex structural elements in practice [4–7].

In 3DCP, the extrusion-based printing process can generally be divided into two processing steps: material deposition and structural build-up [8–12]. This first stage concerns pumping of the printable material from the pump to the printhead, in which material elastic/plastic viscosity is crucial. While pumping, cementitious materials should be continuously transported from the storage system to the nozzle without disruption and blockage, which imposes strict requirement on their fluidity. Within the time frame of an extrusion process, two material properties, namely viscosity and dynamic yield stress, co-determine the material pumpability [13]. When submitted to stresses higher than a critical threshold value (i.e., dynamic yield stress), the printable material therefore flows and behaves approximately as a visco-plastic Bingham fluid [14]. In this context, Computation Fluid Dynamics (CFD) and rheology methods have been adopted for numerical analyses of material flowability [4,15–17]. The second stage describes the buildability (i.e., the maximum number of consecutive layers that can be printed). After material deposition, the printed layers should be stiff enough and strong enough to retain the self-weight and gravitational loading of subsequent layers without excessive deformation or collapse [5]. Below material yield stress, the printed material is therefore at rest after extrusion. Consequently, its elastoplastic properties are more important than viscous-plastic characteristics in this stage [18]. The printing process of cementitious materials is sensitive to printing parameters and schemes, which requires not only understanding of pumpability through e.g., CFD or rheological models, but also for structural modeling or printing trials to quantify the buildability.

In general, predictions of structural integrity are achieved through comprehensive printing trials as well as material property experiments, in which a series of various printing velocities, material mixes, and printed object sizes may be investigated. For a relatively small printing object, the practicality of this approach is debatable due to time and resource restrictions. But when it comes to large-scale objects or a huge number of competing printing parameters this approach is not practical or is even impossible. More currently, analytical and numerical

* Corresponding author.
E-mail address: m.liang-1@tudelft.nl (M. Liang).

https://doi.org/10.1016/j.autcon.2022.104485
Received 16 September 2021; Received in revised form 19 June 2022; Accepted 10 July 2022
Available online 19 July 2022

approaches have shown the feasibility of structural instability analysis, therefore, they might replace (or at least reduce) the need for tedious trials for printing scheme optimization. As illustrated from the printing trials, two competing failure modes are frequently reported: plastic collapse through material yielding and structural instability by local or global buckling [2,15,19]. Plastic collapse failure is characterized by maximum stress of the critical layer reaching the material yield stress, while elastic buckling is determined by a loss of geometrical stability.

In relation to quantification of structure build-up, two types of approaches, consisting of rheological theory and solid mechanics, are commonly adopted to assess, whether and how, printed objects may fail [4,20–26]. In essence, rheological models [13,19,23,27] account for the flocculation-induced thixotropy and chemical phenomena, predicting the critical printing height due to plastic collapse. Significant contributions are from the analytical model of Roussel [13], the experimentally validated lower bound analytical model of Kruger et al. [19,28], the exponential yield stress-curing time model of Wangler et al. [27], and a non-linear model by Perrot et al. [29,30]. Indeed, these models reveal the influence of pseudo-strain hardening and flocculation-driven structuration on the material yield stress, thereby quantifying buildability of 3DCP through material yielding.

However, the above-mentioned rheological methods concern purely strength-based material yielding, whereas structural failure of a printed object is sometimes a result of local or global buckling, as illustrated by printing trials in the literature [9,31,32]. Predicting the buckling response is therefore crucial for structure build-up. Based on solid mechanics, a mechanistic model was proposed by Suiker [20] to quantify buildability of wall-type structures. This model incorporates five critical printing parameters, including printing velocity, geometrical features of the printed object, time-dependent mechanical properties, presence of imperfections, and non-uniform dead weight loading; and it can explore the three basic configurations on plastic collapse and elastic buckling of a wall structure. The model shows a good match with experimental data [20,21]. However, this parametric model is exclusively available for wall-type layouts. For more printing geometries to be broadly analyzed, a finite element model (FEM) accounting for material yielding and structural instability was first developed by Wolfs et al. [21,32] using a commercial software package ABAQUS. Further developments have been reported by other research groups [33–35]. In Wolfs' numerical analyses, an age-dependent Mohr-Coulomb failure criterion was introduced and a correct failure-deformation mode of plastic collapse was reproduced. Regarding elastic buckling, a bifurcation linear buckling analysis was first performed, and numerically derived geometrical imperfections were introduced into the initial model for a non-linear buckling analysis. Consequently, an asymmetric mode of buckling failure can be obtained through nonlinear analyses regarding structural stability of wall and rectangular structures. More recently, a parametric FEM model, allowing for contact-based interactions and a division of printing segments, was proposed by Ooms et al. [33,36], in which a correct buckling failure mode of a structure was reproduced, as well as the critical printing height. This model revealed the importance of non-uniform gravitational loading due to sequential printing process on the structural failure analysis. However, this research work aims at proposing a parametric tool to automatically create finite element models without limitation on geometric complexity and extensive manual modeling, no further explanation associated with failure mechinism and influence of printing parameters on buildability quantification have been put forward in the published literature.

Although current numerical methods can reproduce the correct failure-deformation mode and are in quantitative agreement with experiments in terms of critical printing height, the failure mechanism behind structural instability for 3DCP is still unclear from the numerical point of view. A fundamental understanding associated with all kinds of heterogeneity is essential for structural stability analysis. The heterogeneity indeed presents two aspects for buildability assessment. First, in most analytical frameworks and numerical models, layers of printing objects stacked on top. This disregards the fact that, in practice, each layer is sequentially extruded across the previous one, resulting in non-uniform gravitational loading. Subjected to such loading heterogeneity, element stress may not increase along with printing height. In this case, the critical layer may no longer be the initial one (i.e., the first layer), consequently, most analytical strength-based criteria and current numerical models are no longer applicable. Second, homogeneous isotropic materials are adopted in the previous FEM work of 3D concrete printing [21,33,35], this solution approach ignores the heterogeneity characteristic of printing objects. Due to the heterogeneity of materials, some localized damage might generate and proceed to structural collapse by material yielding in actual printing trials. However, such FEM models fail to account for this kind of failure process.

In order to fill these gaps, a numerical method based on lattice discrete element model was presented to study their influence on printing characteristics [37]. Lattice modeling of two commonly used structures (i.e., hollow cylinder and square structure) was able to reproduce the correct failure-deformation mode, as well as the critical printing height. Nevertheless, the proposed method was only able to consider the failure mode of plastic collapse, while the elastic buckling could not be considered without accounting for geometric nonlinearity.

Herein, based on our previous work [37], geometric nonlinearity is introduced into the lattice model for buildability quantification, especially for buckling response. This modified lattice model incorporates time-dependent mechanical properties, different printing velocities, and printing directions, heterogeneity, localized damage, and non-uniform gravitational loading. Using this newly proposed model, the asymmetric failure of buckling response could be simulated without introducing initial geometrical imperfections. As will be shown, this can be attributed to a combined effect of geometric nonlinearity and system heterogeneity, including mesh randomness of model discretization, localized damage, and printing segment division.

This article is organized as follows. First, Section 2gives a brief model overview, including model discretization, layer division of printing segments, system and element failure criterion. Section 3 then elaborates on how to incorporate geometric nonlinearity into lattice model. Subsequently, the computational uniaxial compression tests are performed to calibrate time-dependent material behaviors in Section 4.1. Based on calibrated age-dependent material properties, stability analyses of two types of structures that are sensitive to buckling response: free wall and rectangular layout, are carried out for model validation in the end.

2. Model overview

2.1. Model discretization

In 3D printing trials, tools of digital design such as building information modeling or computer-aided design have already been developed. Through a computer-controlled positioning procedure, a collective geometry can be created via a layer-by-layer deposition process. In the lattice model, a designed object is first discretized by a network of beam elements, as depicted in Fig. 1. Timoshenko beam elements [38] are adopted here as to account for shear deformation, given the low ratio between element length and cross-sectional dimensions.

When it comes to detailed procedures of model discretization, a cubic domain is first divided into a series of cubic grids with a specific cell size, which is defined as the mesh resolution. Then a sub-cell is generated within each cell. The ratio between the size of sub-cell and cell, defined as randomness, allows for mesh disorder [38–42]. As the third step, a pseudorandom number generator is used to randomly place the lattice nodes within each sub-cell domain. This is then followed by Delaunay triangulation to define the element connectivity [43], as shown in Fig. 1b and Fig. 1c. In this step, the volumes of individual Voronoi cells, each of which corresponds to a single node in the mesh, are calculated. These volumes are used to determine the magnitude of gravitational

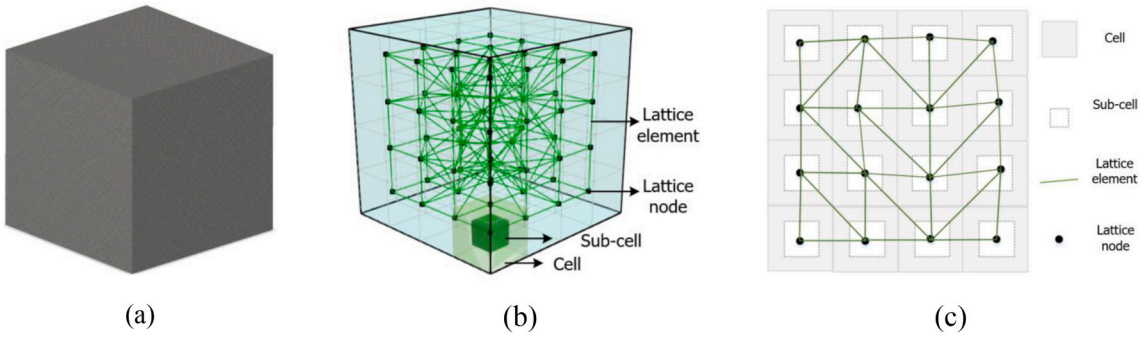

Fig. 1. Schematic view of lattice model establishment (a) Analysis object (b) Lattice mesh in 3D (4 × 4 × 4) (c) Element connectivity in 2D (4 × 4).

loading acting in each node, as described in detail in our previous work [37]. Since printable materials are not completely homogeneous, mesh disorder can mimic system heterogeneity from a model discretization point of view [41,44–47].

2.2. Layer division

In printing trials, cementitious materials are extruded continuously from the nozzle and placed on top of the previous layers, which leads to non-uniform gravitational loading in the printing system. To accurately model the actual printing trials (see Fig. 2a), each layer of a designed object (see Fig. 2b) is composed of a series of printing segments in the present model (as indicated in Fig. 2c). These divided layers and segments, labeled with different initial time, characterize the subsequent printing process, revealing the influence of non-uniform gravitational loading on structural instability analysis. Additionally, an element birth technique is utilized to evaluate, when and where, the relevant printing segments are activated in the structural analysis of the printing process. Considering material behavior, the lattice beam elements belonging to different segments are assigned with time-dependent material properties at each step, reflecting material stiffness and strength development during printing.

2.3. Element failure criterion

During the manufacturing process, there is a 'competition' between non-uniform gravitational loading and time-dependent material properties [15,48]. To be specific, on the one hand, the gravity-induced stress of printing filament generally increases as subsequent layers are added to the printed structure; the material yield stress, on the other, also increases (linearly or exponentially) with the printing process, as does the elastic modulus [19,23,27]. If the yield stress is reached in any point in the printing object, localized damage occurs, similar to the crack initiation in hardened concrete. In most cases, the localized damage will result in weaker load-bearing capacity of the 3D printed system, thereby accelerating the structural failure, as it might coincide with extensive deformations, progressive collapse, and cracking [5,13].

In the lattice model, an element-removal mechanism is employed for simulation of localized damage in printing process. Subjected to gravity loading and boundary conditions, a set of linear analyses are carried out for stress calculation in the beam elements. In relation to element failure criterion, the normal force and the bending moment are considered, mathematically as follows:

$$\sigma = \alpha_{\mathrm{N}}\frac{F}{A} + \alpha_{\mathrm{M}}\frac{\left(|M_i|, |M_j|\right)_{\max}}{W} \qquad \sigma_{yield} \le \sigma \tag{1}$$

where F is the normal force subjected to lattice beam element; M_i and M_j are the nodal bending moments in local coordinate, respectively; A the element cross-section and W is the cross-sectional factor for bending resistance, referring to the circle cross-section, $W = \pi D^3/32$ (D is the diameter of lattice element, which is assumed equal for all elements). The parameters α_{N} (i.e., normal force factor) and α_{M} (i.e., bending influence factor) codetermine the proportion of these two forces, governing element failure in which either normal force or bending moment plays a dominant role. Building upon the previous research, α_{N} is adopted as 1.0 [49–51] and α_{M} value is set to 0.05 [37,47,49]. After each analysis step, multiple critical elements, i.e., those in which the element stress exceeds the material yield stress, are removed from the mesh.

2.4. Structural failure criterion

In 3DCP experiments, when a relatively large offset occurs between the uppermost printing layer and the designed position, the new printing segment cannot be deposited into the designed position with sufficient accuracy. Consequently, the printed object might be unstable and eventually fail due to the material yielding or structure buckling.

In this numerical campaign, the gravity-induced stress increases with deposition process, generating more broken elements. The printing

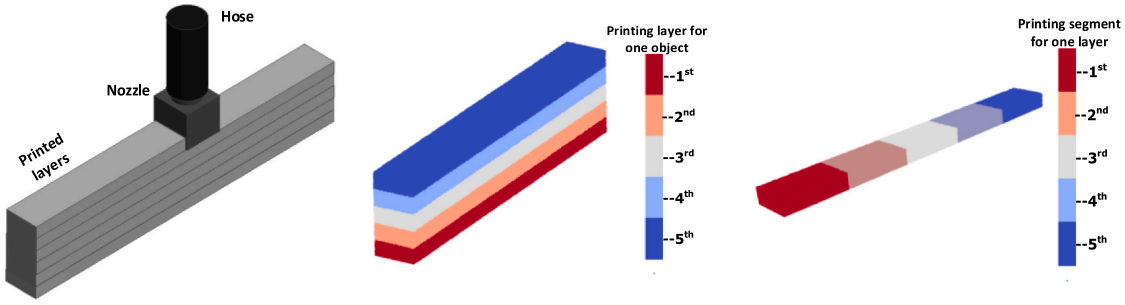

Fig. 2. Schematic view of printed object in design and lattice model generation (a) printed object in design (b) printed object in lattice (c) layer division.

process can then be regarded as failed, providing the offset between design and actual position is equal to or higher than the width of an individual layer, as described in Fig. 3. This failure criterion is in accordance with experimental findings and avoids an underestimation of critical printing height [37].

3. Geometric nonlinearity

Our previous lattice model for 3DCP could reproduce the plastic collapse failure mode and is in quantitative agreement with experimental data [37]. However, it was not applicable to elastic buckling, considering the failure mechanism is generally induced by local or global geometrical stability. Therefore, assessing structure failure of elastic buckling might be possible if geometric nonlinearity is introduced into the lattice model [21].

3.1. Theoretical framework

In this research, the implementation of geometric nonlinearity considers kinematic descriptions in principle while physical non-linearity due to material development is considered through updating the material stiffness matrix. By means of virtual displacement formula and second-order elastic analysis, the effect of finite deformations and displacements in structural analysis can be accounted for through the following equations [52,53],

$$\begin{aligned} &\left(K_t + K_g\right)\Delta D = \Delta F \\ &\Delta F = F_{ex} - F_{in} \end{aligned} \tag{2}$$

In which the $\boldsymbol{\Delta F}$ and ΔD are incremental loading and displacement of printing system, respectively. For structural analysis of 3DCP, this incremental force can be computed based on external load F_{ex} and internal element force F_{in}.

In the model, K_t, is the material stiffness matrix, dependent on Young's modulus (E) (transient material properties during printing process) and B_L (strain-displacement relation), which is computed based on strain condition and interpolation function (as described in eq. (3)). More specifically, G includes the differentials towards every strain measure and condition while H contains the interpolation function. The geometric stiffness matrix K_g is updated on the basis of kinematic descriptions and derived element force after each analysis step; the C_t represents 2nd Piola-kirchoff stress in matrix form, and B_{NL} is the shape function in non-linear form considering incremental loading, mathematically described as follows [52].

$$\begin{aligned} B_L &= GH \\ K_t &= \int_0^l B_L^T E B_L^T dx \\ K_g &= \int_0^l B_{NL}^T C_t B_{NL}^T dx \end{aligned} \tag{3}$$

3.2. Numerical implementation

The pre-processing procedures of the numerical analysis have been described in Section 2 and the corresponding solution flowchart concerning geometric nonlinearity will be explained in this section. The extended lattice model with geometric nonlinearity for buildability quantification of 3DCP encompasses six branches: A, B, C, D, E and F, as indicated in Fig. 4.

In this flowchart, the $\boldsymbol{k}$ and $\boldsymbol{K}$ stand for local and global stiffness matrix, respectively. To be specific, subscripts 't' and 'g' refer to material stiffness and geometric stiffness matrix. The $\boldsymbol{T}$ is the transpose matrix transferring the local domain to the global domain. The $\boldsymbol{L}$ and $\boldsymbol{D}$ are the global load and displacement vectors, respectively. The subscript i^{th} stands for the analysis step. Also, $\boldsymbol{\sigma}$ and $\boldsymbol{\Delta\sigma}$ are the cumulative element stress and incremental element stress within one step analysis, so does the cumulative node displacement $\boldsymbol{\delta}$ and incremental node displacement $\boldsymbol{\Delta\delta}$. The $\boldsymbol{F}$ refers to load vector, and subscript 'ext' and 'int' stand for the external load due to gravitational loading and internal load stored in the printing system derived from the last known equilibrium stage. The $\boldsymbol{\Delta F}$ is derived disequilibrium force between external load and internal load.

Branch A: Modeling procedure.

A brief introduction has been given in Section 2, and detailed information can be found from previous research [37].

Branch B: Update printing time and activate new printing segments considering geometric nonlinearity.

B1: In the lattice model, layers of a printed object can be subdivided into different segments, allowing for sequential printing process. These time-based segments will be activated immediately once the predetermined time is reached. They are, subsequently, assigned with material behaviors, which grow in a linear or an exponentially decaying fashion. For instance, if the interval period between two segments takes 1 min; after 5 segments, the initial one is characterized by 5-min material properties, the 3rd printing segment also is assigned with 3-min old stiffness and strength, and so on.

B2: Once transient material properties are assigned to corresponding elements, the element stiffness matrix $\boldsymbol{k}$ in local domain can be assembled. Combined with transposed matrix $\boldsymbol{T}$, the global tangent stiffness

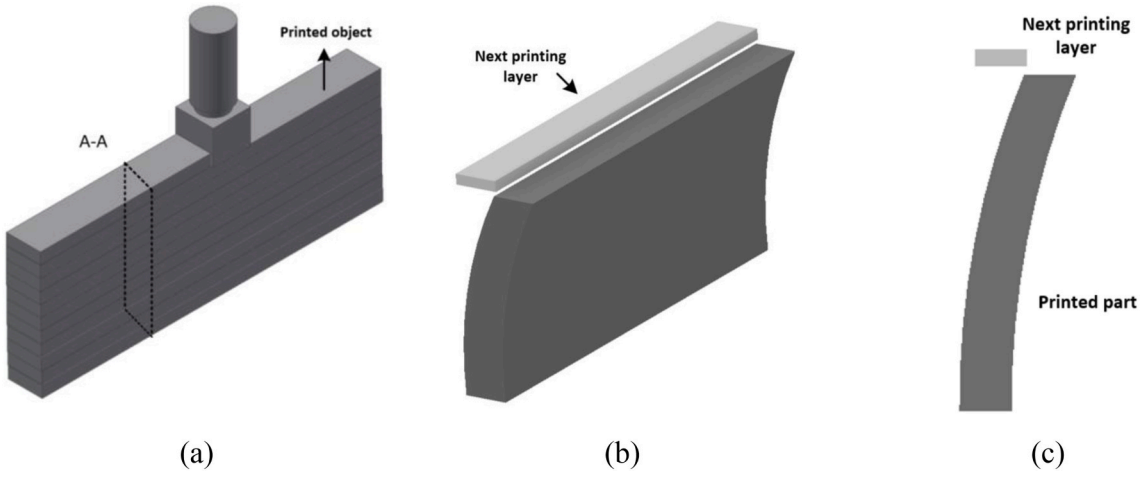

Fig. 3. Structure failure criterion in lattice model for 3DCP (a) Continuous printing process (b) Failure mode in 3D (c) Failure in 2D.

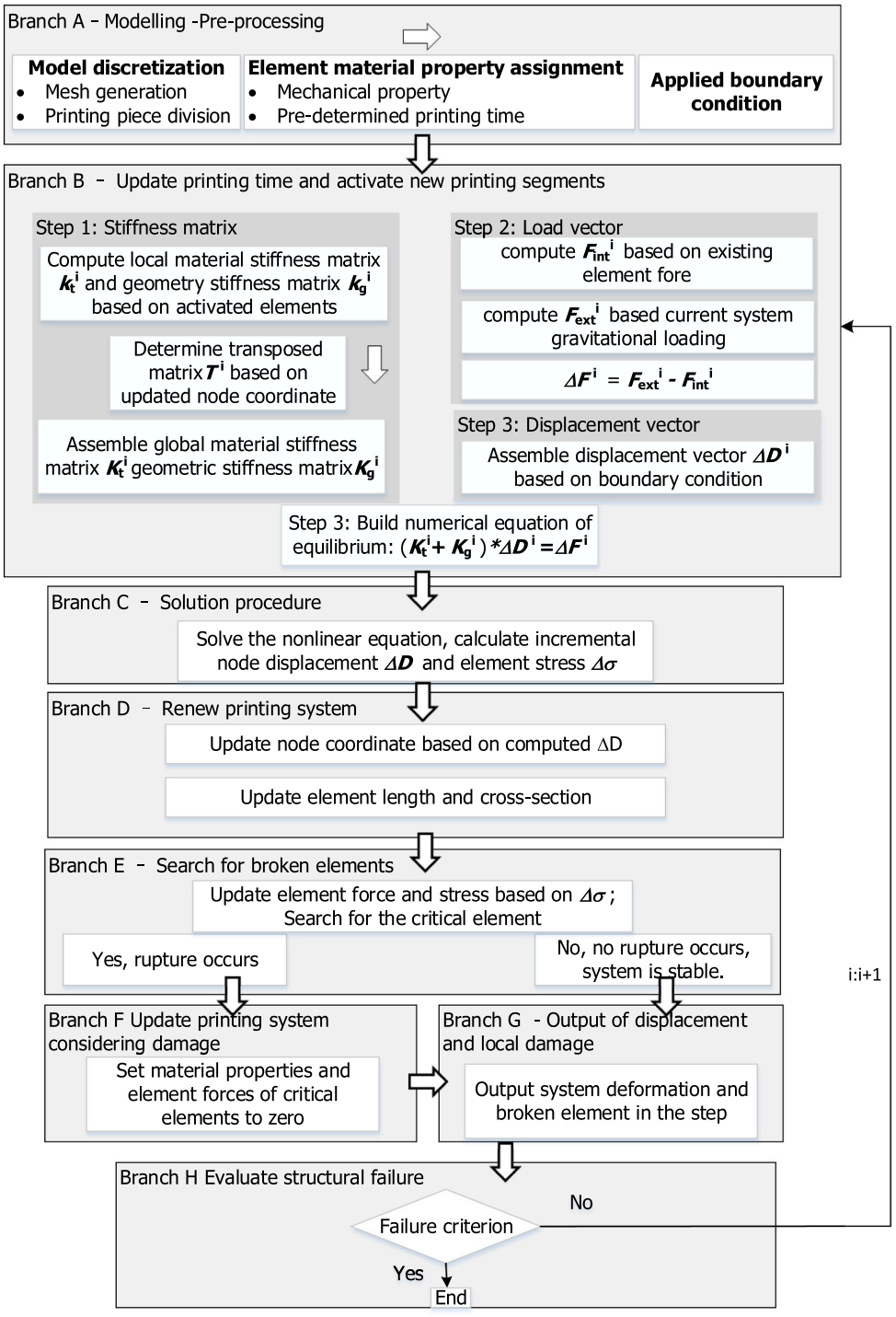

Fig. 4. Implementation of geometric nonlinearity in the lattice model.

matrix $\boldsymbol{K_t}$ and geometry stiffness matrix $\boldsymbol{K_g}$ of each activated element can also be derived, as mathematically expressed in the Eq. (4). Typically, the $\boldsymbol{K_t}$ is a linear elastic component and determined by transient material properties while $\boldsymbol{K_g}$, the geometry stiffness matrix, is relevant to the 2nd Piola-Kirchoff stress and calculated based on element force, as discussed above.

$$K_g = T^T k_g T$$
$$K_t = T^T k_t T \quad (4)$$

Branch C: Solve the nonlinear eq.

C1: The numerical analysis of printing process is based on lattice model using an updated Lagrangian method and the numerical equation of equilibrium (i.e., eq. (2)) is solved using the midpoint Runge-Kutta method [53]. A parallel computation approach has been adopted for computing efficiency, clearly showing model feasibility for large scale structural analysis.

Branch D: Renew printing system based on solved displacement.

D1: The node coordinates are updated as well on the basis of obtained $\Delta\boldsymbol{D}$ using updated Lagrangian method. Then, the element length is recalculated based on new node coordinate, and the cross-section is updated considering constant element volume.

Branch E: Search for broken elements & Branch F: update printing

system considering localized damage.

After the solution procedure, derived nodal displacement are utilized for determining the elemental stresses. Afterwards, critical elements are immediately removed from mesh system according to the element failure criterion (Eq. (1)), and their internal forces are also released.

Branch G: Output structure deformation and localized damage after one-step analysis.

Branch H: Evaluate system failure.

H1: In the numerical procedure, the numerical analysis of buildability quantification will be performed until the structural failure criterion (as described in Section 2.4) is reached. For each step analysis, the next printing segments is placed on the designed/original position instead of being adjusted along with deformed geometry, and this solution method is in accordance with actual trails [31,35]. As soon as the next printing segment is successfully placed on the top of the current system, the printing process will proceed, in which the printing time updates and a new printing segment is activated.

In the next analysis step, the deformed shape is utilized as the reference frame and the incremental equation will be built here with relation to Updated Lagrangian formulation [54]. It should be mentioned that a series of parameters, including stiffness matrix, external and internal loading, must be updated based on this reference geometry.

The necessity of matrix modification, consisting of stiffness matrix $\boldsymbol{K_t}$ and geometry matrix $\boldsymbol{K_g}$, is also required given deformed structure. On the one hand, presence of localized damage produced in the previous analysis step reduces the material properties of critical elements to zero, which is detrimental to the printing system; the sequential printing process, on the other hand, activates more printing segments and linearly or exponentially enhances the material properties of existing elements. The geometric stiffness matrix allowing for the effect of geometry loss on structure analysis, and material stiffness standing for localized damage and material development, are computed based on the element force, updated material properties and deformed structure. The contradictory effect of material development and occurrence of localized damage results in uncertain prediction of buildability and their influence will take effect in next step analysis.

The load vector of internal force also renews after each step, which can be attributed to two aspects. First, the incremental gravitational loading is applied on the system, which causes the element internal forces to evolve. Second, the updated transpose matrix T results in orientation variation of beam elements, leading to a different internal load force vector in the global domain.

After renewing all above-mentioned parameters, the numerical analysis of buildability quantification will be continuously performed to assess when and how the printed object fails.

4. Numerical model

In this section, we perform numerical analyses of structural instability through two layouts sensitive to buckling failure: a free wall and a large square structure [31,32], as indicated in Fig. 5. In relation to buildability quantification, computational uniaxial compression tests are first performed to calibrate essential material behaviors such as stiffness and strength [31,32]. The calibrated material properties are subsequently employed for structural build-up in which failure-deformation mode, as well as critical printing height, is predicted. Herein, this study adopted experimental campaigns, including material tests and 3D printing trials, from Wolfs et al. [31,32] for model calibration and validation.

4.1. Model calibration: computational uniaxial compression test

In this study, the uniaxial compression tests from the literature [35] is utilized to calibrate model parameters. The 'green strength', allowing fresh concrete to withstand self-weight or loading from subsequent layers, is usually measured using an unconfined uniaxial compression test. In this study, two types of materials are employed for 3DCP: material A for the free wall structure and the material B for the square layout. Considering that experimental campaigns of green strength use different materials, two common features are 'experiment setting' and 'boundary condition', as both are key factors for material properties determination. In the green strength test, a double sheet of Teflon is placed on the two sides of specimen to reduce friction, and specimens with various curing times are then tested in uniaxial compression using a displacement-controlled loading, and the details can be found from [35]. However, another dominant characteristic of prepared samples is a compaction process, which plays a significant role on the measured material properties. On the one hand, the samples which use material A have been cast into steel cylindrical molds without compaction, probably resulting in similar material properties as those in the actual printing process, in which the material is extruded; specimens of material B, on the other, underwent compaction process through by a vibrating table [35], which may be somewhat different compared to the actual printing process. The previous research indicates a significant difference of strength and stiffness due to the compaction process [32], as discussed later.

Concerning the computational uniaxial compression test, cylindrical samples with 5 mm mesh resolution are built to characterize age-dependent mechanical properties using lattice model. To mimic the boundary conditions occurring in printing trials, two sides of the cylinder model are allowed to freely move in the radial direction; nodal displacements on top edge are then applied to system along with vertical direction while the bottom edge was fixed. With respect to material yield stress in the element failure criterion, compressive and tensile strength of lattice elements have been adopted as the yield stress of printing

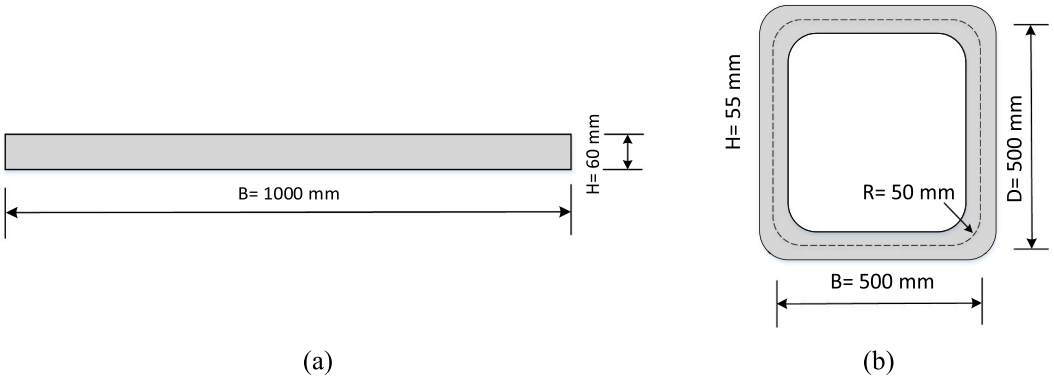

Fig. 5. Geometrical characteristics of the free wall and rectangular structure for 3DCP (a) free wall structure (b) rectangular layout, both viewed from the top.

material in accordance with the maximal stress theory [20,31]. Furthermore, the compressive strength is taken as 10 times as high as tensile strength, reflecting a stronger capacity for compression behavior. Note that the calibration process is based on previously published research generally associated with hardened cementitious materials and may need to be reassessed in the future [47].

The computational uniaxial compression tests were carried out for specimens under each age tested in the literature [31,32]. The calibrated elastic modulus and compressive strength were listed on Table 1, in contrast to experimental results. In 3DCP, plastic collapse is largely dependent on the material strength, while buckling failure mode is strongly dependent on the material stiffness. Thus, in contrast to the material strength, the material stiffness is more important in predicting structure instability due to buckling. Thus, the material plastic behavior is not taken into account during the calibration process. The calibrated numerical results are in excellent agreement with the experimental findings, which proves this numerical model has accurately derived material stiffness and strength of fresh concrete. These time-dependent material properties are therefore adopted and then can be utilized for formulation of curing function. Two time-dependent material properties, i.e., a linear and an exponential relationship, are often adopted for time-dependent material properties. Considering the exponential yield stress evolution can describe a smooth transition from initial linear increase to exponential evolution [23,25], it is adopted herein to describe age-dependent material properties (i.e., elastic modulus and compressive strength). It should also be noted that some experimental results show considerable scatter, which is attributed to the compaction process. The material usually does not undergo a compaction procedure during the printing process. However, green strength tests on the material B are conducted after a compaction process. The published research indicates [32] that there is a difference between samples subjected to a compaction process and those ones that are not. The influence becomes more pronounced with concrete age. Thus, the aging time above than 30 min is not taken into account during calibration process. Here, the material A without compaction process enables to identify curing function according to all calibrated results, while regarding material B only transient material properties under 15 and 30 min are adopted for material development to eliminate experimental scatter induced by compaction process. This identified material development will be taken as time-dependent material properties for structure analysis of bucking response in next section. This is no doubt that the fitting function of time-dependent material properties would be more reliable given more available data. A possible way to accomplish this is to perform green strength tests without compaction. However, this is beyond the scope of the current work. On the basis of calibrated material properties listed in Table 1, the time-dependent material behaviors of lattice elements can be described as Eq. (5) and (6).

$$\begin{aligned} E_c^A &= 55.97e^{0.0142t} \\ f_c^A &= 22.76e^{0.0127t} \end{aligned} \tag{5}$$

Table 1
Calibrated mechanical properties with a range of time 0 to 90 min.

Material type		Input material properties in lattice model		Computational uniaxial compression test	
A	Concrete age (min)	Young's modulus (kPa)	Compressive strength (kPa)	Young's modulus (kPa)	Compressive strength (kPa)
	15	60.20	7.35	60.20	7.29
	30	104.08	10.00	104.08	9.97
	60	128.57	12.86	128.57	12.71
	90	197.96	20.92	197.96	20.87
B	15	101.41	8.05	101.41	7.89
	30	135.21	12.37	135.21	12.62

$$\begin{aligned} E_t^B &= 76.31e^{0.019t} \\ f_t^B &= 11.10e^{0.0458t} \end{aligned} \tag{6}$$

where the E represents the elastic modulus, determining the elastic deformation; f_c stands for the material compressive strength.

4.2. Model validation

4.2.1. Free wall structure

Model validation of buckling response starts from a free wall structure printed with material A, the dimensions of which are 1000 mm length and 60 mm width in print trials [32]. The printing velocity equal to 6250 mm/min was employed to exponentially develop material behaviors. The detailed information about this free wall structure is given in Table 2.

Prior to structural analysis of buckling failure, each printing layer, including 4000 lattice nodes connected by around 35,000 Timoshenko beams, is divided into three printing segments to study the impact of non-uniform gravitational loading based on previous research [37]. It means that sequential printing segments are continuously added alongside each other with a time frame of numerical analysis, as described in Section 2. Rather, mesh resolution of 5 mm, which is line with computational uniaxial compression test, has been characterized for the purpose of elimination of size effect on buildability quantification. The 10 mm of layer height is therefore adopted in this numerical analysis, a little bit different with experiment with 9.5 mm. fully fixed support was utilized on the bottom to capture high friction caused by printing bed in the trials. In terms of loading condition, nodal forces representing gravitational load are determined by the material density (2100 kg/m^3) and the volume of each Voronoi cell, as described above. One point should be noted, unlike the FEM analyses of buckling failure in 3DCP discussed above, no geometric imperfection is introduced into the printed object in advance. The structure failure due to elastic buckling is therefore a combined effect of localized damage and non-uniform gravitational loading due to sequential printing process.

The typical failure mode of free wall structure is depicted in Fig. 6, indicating this failure-deformation mode is dominated by elastic buckling. Fig. 7 provides the comparison of localized damage before and after structure failure. In relation to the critical printing height, failure occurred at 18th layers, while no excessive deformation could be observed before the final failure, as illustrated from Fig. 6a. While the material yielding, a few broken elements, standing for localized damage, can be observed from Fig. 7a. This is attributed to the combined effect of heterogeneity consisting of non-uniform loading and mesh randomness, in accordance with localized damage of a printed object during an actual process. Further exploration goes to failure process and mechanism observed from the numerical analysis: although homogeneous material properties are assigned to lattice elements, the printed object still shows strong heterogeneity caused by the random lattice mesh and non-uniform application of gravitational load (i.e., division of printing segments). This expedites localized damage and loss of geometrical stability, in which the former governs the plastic collapse while the latter is crucial for elastic buckling. Under the effect of system buckling, a growing number of broken elements also can be observed from Fig. 7b.

In comparison with experimental results in the literature [32], this model not only reproduces the experimentally derived failure-

Table 2
Printing process parameters for wall structure.

Parameter	Value
Wall thickness (mm)	60 mm
Concrete density (kg/m^3)	2100
Printing velocity (mm/s)	6250 mm/min
Initial material stiffness (kPa)	55.97 kPa
Initial material strength (kPa)	22.7 kPa

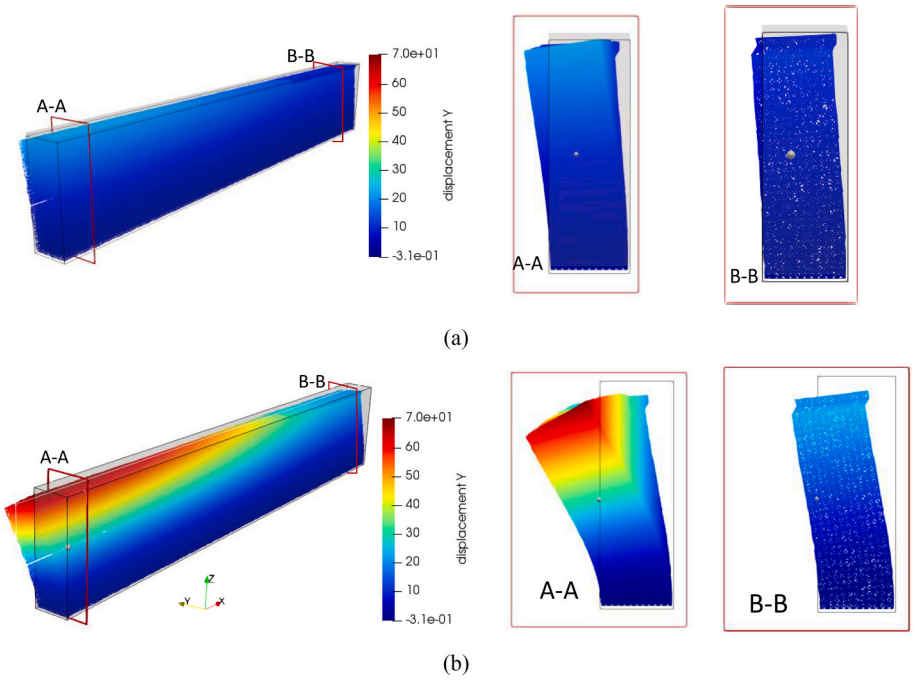

Fig. 6. Failure by elastic buckling of a free wall structure (a) before failure (b) after failure.

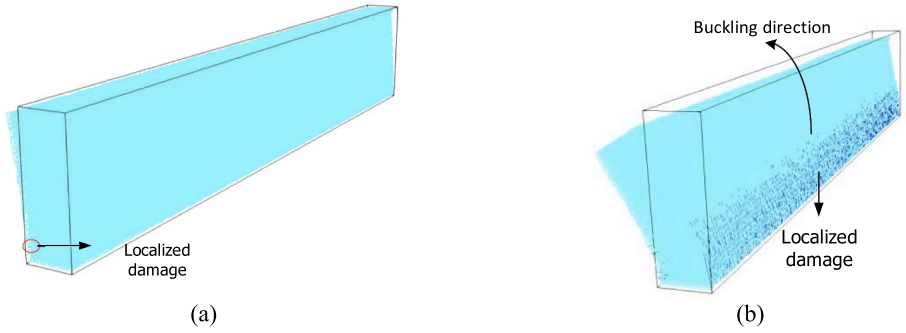

Fig. 7. Localized damage (shown in black) for wall structure (a) before failure (b) after failure.

deformation mode accurately without introducing initial geometric imperfections, but also predicts the experimental results well in quantitative terms. Specifically, when placing 18th layer into origin position, the offset between the design position and deformed geometry is larger than the width of individual layer. It can be observed that the final failure occurred at 18th layer, and the critical printing height is 180 mm, around 12% lower than the test data (i.e., 204.25 mm). A deviation of up to 20% is not exceptional, considering that the input material properties are calibrated by uniaxial compression experiments, where significant scatter exists (i.e., the relative standard deviations up 21% for elastic modulus and around 17% for the yield stress).

4.2.2. *A large square structure*

In this section, the dimension of square structure, side = 500 mm and width = 55 mm, was modeled through material B under exponential material evolution [31], the relevant parameters are listed in Table 4. Each layer of square structure, consisting of 8000 lattice nodes connected by around 61,000 Timoshenko beams, includes four segments to coincide with the continuous printing process. Like the above modeled free wall structure, a fully fixed boundary condition and the same solution of nodal force have been employed, as well as the mesh fineness. Similar to wall structure, no initial geometric imperfection is introduced for numerical analysis of structure stability.

The typical failure mode of a square structure is shown in Fig. 8, and comparison with experimental data associated with printing height is indicated in Table 3. Fig. 9 provides the comparison of localized damage before and after structure failure.

Regarding failure process, dead weight of the stepwise increasing layers induced some damage near to the bottom (as indicated in Fig. 9a), thereby exacerbating structural instability. The rectangular structure fails after the 23rd printing layer due to out-of-plane displacement in A-A plane, predicting critical printing height equal to 230 mm. Meanwhile, significant localized damage can be observed near to the buckling zone, as depicted in Fig. 9b. In contrast to experimental result with 261.125 mm, a deviation around 12% can be derived, which is less than 20%. It is therefore concluded that the model for the square structure not only can reproduce the correct buckling-dominant failure mode, but also that the critical printing height is quantitative agreement with the experiments.

4.3. *Discussion*

The above numerical analyses indicate that the extended lattice model enables correct simulations with respect to structural failure of buckling response, qualitatively similar to printing trials in the literature [31,32]. In relation to the critical printing height computed for these two structures, deviations of 11.87% and 11.97% were derived for

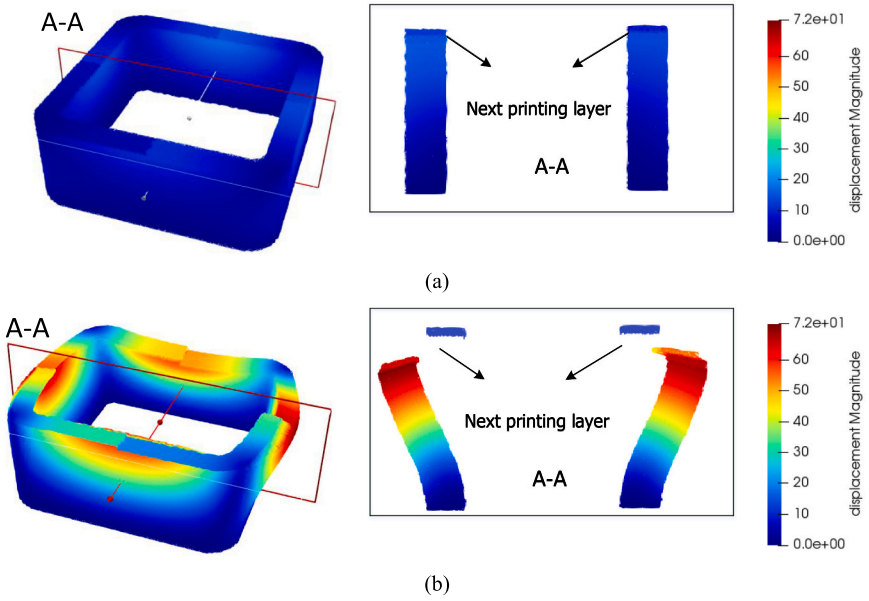

Fig. 8. Failure by elastic buckling in the numerical analysis of rectangular layout structure (a) before failure (b) after failure.

Table 3
Experimental value and model prediction of the critical printing height for free wall and rectangular structure.

Printed sample	Experiment	Lattice model	Relative difference
Free wall	204.25 mm	180 mm	−11.87%
Square structure	261.14 mm	230 mm	−11.92%

respectively of free wall and square layout.

When it comes to the failure process, some localized damage first occurs, detrimental to structural stability. Subjected to heterogeneity, including mesh randomness and non-uniform gravitational loading, numerical models are likely to fail because of combined failure mode, here the elastic buckling plays a dominant influence. Meanwhile, this kind of buckling response also causes more localized damage to printed systems in return, as observed from Fig. 7b and Fig. 9b. It can be concluded that structural failure of 3d printing is a complex combination of plastic collapse and elastic buckling. Assessing build-up performance of printed system merely considering one of them will likely result in errors since their interaction, which actually exists in print trials, is ignored.

In this study, a comparison between the numerical analyses and experimental results strengthens the necessity to correctly characterize the behavior of printing materials. Specifically, time-dependent material behaviors of 3D printed concrete are characterized through uniaxial compression test, in which up to 20% material variation has been experimentally reported [31,32]. Considering that structural analyses of printed objects are performed based on the average material stiffness and strength of green strength tests, the deviation on buildability quantification around 12% can be considered an excellent quantitative agreement.

Nonetheless, the critical printing heights computed from lattice model are lower than those in actual print trials in both validation cases. This suggests that there are some effects that are not incorporated into numerical analyses which may positively affect on build-up performance. Three possible reasons may be hypothesized. First, the material stiffness and strength experimentally established by green strength test in the literature might be lower than real values in 3D printing trials due to the compaction influence, especially for material B. Besides, the unconfined compression test is utilized to characterize material stiffness, while a fully fixed boundary condition is employed in printing trials. In

Table 4
Printing process parameters for square layout.

Parameter	Value
Wall thickness (mm)	55
Model length/B (mm)	500
Model width/D (mm)	500
Concrete density (kg/m^3)	2100
Printing velocity (mm/s)	83.3
Initial material strength (kPa)	11.10
Initial material stiffness (kPa)	76.31

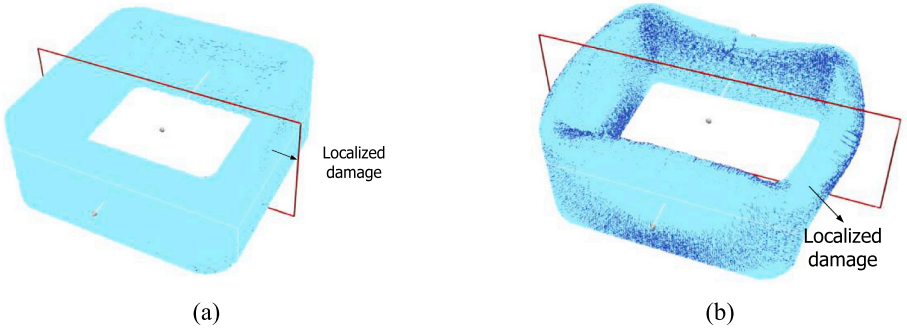

Fig. 9. Localized damage for square structure (a) before failure (b) after failure.

reality, low friction in terms of boundary condition might cause a reduction in material stiffness [9].

The 3D printing process also causes the material to warm up, which is ascribed to the friction in the mixer-pump and the hose. Consequently, the heating history may influence the mechanical and rheological behaviors [55] due to speeding up of the hydration process, especially for the larger objects with a longer printing process. More recently, an outcome of the ultrasound tests conducted by Wolfs et al. [32] also shows an influence of temperature on structural properties of 3D printing materials at the early age.

The time-dependent deformation at early stage, consisting of shrinkage and creep, may also affect the structural stability by means of stress redistribution and local deformation. But to the best of our knowledge, the influence of early-stage shrinkage and creep on buildability has yet to be explained. More experimental research work is essential to be first performed for behind mechanism or input parameters of numerical analyses.

5. Model limitation and extension

In this research, the geometric nonlinearity has been incorporated into lattice model Combined with different features of heterogeneity, the structural instability of buckling response can be reproduced and quantitative agreements with experimental data also can be computed by the extended lattice model.

In contrast to FEM analysis of Wolfs et al. [21,32], this model can reproduce the buckling failure without a bifurcation analysis or introducing initial geometrical imperfections. It reveals that the buckling response is a combined effect of system heterogeneity and geometry loss during printing process. Furthermore, for both geometries used for validation, the experimentally observed asymmetry of failure mode can be derived without introducing any initial geometric imperfection; the structural failure due to elastic buckling is attributed to the combination effect of localized damage, geometric nonlinearity, non-uniform gravitational loading and geometry disorder of material texture.

Regarding the model limitation and extension, the updated Lagrangian method and linear elastic assumption have been adopted for solution procedure and material properties, and the structural instability can be simulated through this extended lattice model. But the rheological behaviors are difficult to consider. Meanwhile, the viscoelastic properties of fresh 3D printed concrete, including early-age creep and shrinkage, also cannot be simulated using this model. However, more recently, several numerical methods, including experimentally informed lattice model proposed by Gan et al. [56], and lattice modeling the drying shrinkage proposed by Gao et al. [57], showcase the possibility to incorporate the viscoelastic behavior into this 3D printing model.

Although some protentional solutions for time-dependent deformation at early ages have come out in terms of numerical analyses, nonexistent literature experimentally reveals the behind mechanism and their impact on buildability quantification; a comprehensive study of these factors is a topic of ongoing research and the corresponding analyses will also be incorporated into lattice model in the future.

6. Conclusions

This study incorporates geometric nonlinearity into the lattice model to quantify the buildability of printing objects by considering the elastic buckling failure mechanism. The computational uniaxial compression tests were first carried out to calibrate the time-dependent material properties. Subsequently, two buckling-sensitive geometries, a free wall structure and a rectangular layout, were adopted for model validation. Based on the results presented, a number of conclusions and novel points are summaries below:

- In 3DCP, several heterogeneity characteristics of printing objects affect structural stability. When subjected to non-uniform gravitational loading, some localized damage due to material yielding might occur to the printing objects with geometry disorder, thereby expediting structural failure. To study their impact on buildability quantification, these heterogeneities should be incorporated into numerical or analytical models.
- This newly proposed model considers a series of printing parameters, including time-dependent material property, printing velocity, localized damage, geometry disorder of material texture, and non-uniform gravitational loading. Using this model, the asymmetric buckling failure mode can be reproduced without introducing any initial geometrical imperfection and bifurcation linear buckling analysis, which are of necessity for published FEM-based models for buildability quantification in 3DCP.
- Lattice modeling of printing objects is not only able to reproduce experimentally derived failure modes qualitatively, but also to agree quantitatively with experimental results.
- During model validation, some discrepancy between numerical predictions and experimental results is observed. This can be attributed to underestimated material properties, temperature influence and early-age material behavior. This results in differences between the data used for the input (i.e., measured on cast specimens) and the real (i.e., extruded/printed) material properties. It may be useful to devise a better testing methodology that considers the intricacies of the 3D printing process and their influence on the mechanical properties.

This research work demonstrates that structural failure through elastic buckling for 3DCP can be reproduced by considering geometry disorder and non-uniform gravitational loading using lattice model with geometric nonlinearity instead of introducing initial geometric imperfections. Together with our previous research work, two failure modes, elastic buckling and plastic collapse, can be reproduced using the lattice model for buildability quantification. In further research, other factors such as early-stage shrinkage and creep will also be incorporated into the model to consider their effects on the early-age behavior of 3D printed concrete.

Declaration of Competing Interest

The authors declare that they have no known competing financial interests or personal relationships that could have appeared to influence the work reported in this paper.

Acknowledgements

Ze Chang and Minfei Liang would like to acknowledge the funding supported by China Scholarship Council under grant number 201806060129 and 202007000027. Branko Šavija acknowledge the financial support of the European Research Council (ERC) within the framework of the ERC Starting Grant Project “Auxetic Cementitious Composites by 3D printing (ACC-3D)”, Grant Agreement Number 101041342. The authors are grateful to Lu Cheng of the Delft University of Technology, Jinwei Ma of Dalian University of Technology for the useful discussions on geometric nonlinearity, their support is gratefully acknowledged.

References

[1] M.S. Khan, F. Sanchez, H. Zhou, 3-D printing of concrete: beyond horizons, Cem. Concr. Res. 133 (2020), 106070, https://doi.org/10.1016/j.cemconres.2020.106070.
[2] F. Bos, R. Wolfs, Z. Ahmed, T. Salet, Additive manufacturing of concrete in construction: potentials and challenges of 3D concrete printing, Virtual Physical Prototyp. 11 (3) (2016) 209–225, https://doi.org/10.1080/17452759.2016.1209867.
[3] S. Lim, R.A. Buswell, T.T. Le, S.A. Austin, A.G. Gibb, T. Thorpe, Developments in construction-scale additive manufacturing processes, Autom. Constr. 21 (2012) 262–268, https://doi.org/10.1016/j.autcon.2011.06.010.

[4] V. Mechtcherine, F.P. Bos, A. Perrot, W.L. da Silva, V. Nerella, S. Fataei, R.J. Wolfs, M. Sonebi, N. Roussel, Extrusion-based additive manufacturing with cement-based materials–production steps, processes, and their underlying physics: a review, Cem. Concr. Res. 132 (2020), 106037, https://doi.org/10.1016/j.cemconres.2020.106037.

[5] R.A. Buswell, W.L. da Silva, F.P. Bos, H. Schipper, D. Lowke, N. Hack, H. Kloft, V. Mechtcherine, T. Wangler, N. Roussel, A process classification framework for defining and describing digital fabrication with concrete, Cem. Concr. Res. 134 (2020), 106068, https://doi.org/10.1016/j.cemconres.2020.106068.

[6] E. Lloret-Fritschi, T. Wangler, L. Gebhard, J. Mata-Falcón, S. Mantellato, F. Scotto, J. Burger, A. Szabo, N. Ruffray, L. Reiter, From smart dynamic casting to a growing family of digital casting systems, Cem. Concr. Res. 134 (2020), 106071, https://doi.org/10.1016/j.cemconres.2020.106071.

[7] C. Menna, J. Mata-Falcón, F.P. Bos, G. Vantyghem, L. Ferrara, D. Asprone, T. Salet, W. Kaufmann, Opportunities and challenges for structural engineering of digitally fabricated concrete, Cem. Concr. Res. 133 (2020), 106079, https://doi.org/10.1016/j.cemconres.2020.106079.

[8] A. Perrot, A. Pierre, V. Nerella, R. Wolfs, E. Keita, S. Nair, N. Neithalath, N. Roussel, Mechtcherine, from analytical methods to numerical simulations: a process engineering toolbox for 3D concrete printing, Cem. Concr. Compos. 122 (2021), 104164, https://doi.org/10.1016/j.cemconcomp.2021.104164.

[9] R. Wolfs, F. Bos, T. Salet, Hardened properties of 3D printed concrete: the influence of process parameters on interlayer adhesion, Cem. Concr. Res. 119 (2019) 132–140, https://doi.org/10.1016/j.cemconres.2019.02.017.

[10] V.N. Nerella, S. Hempel, V. Mechtcherine, Effects of layer-interface properties on mechanical performance of concrete elements produced by extrusion-based 3D-printing, Constr. Build. Mater. 205 (2019) 586–601, https://doi.org/10.1016/j.conbuildmat.2019.01.235.

[11] V.N. Nerella, M. Krause, V. Mechtcherine, Direct printing test for buildability of 3D-printable concrete considering economic viability, Autom. Constr. 109 (2020), 102986, https://doi.org/10.1016/j.autcon.2019.102986.

[12] Y. Chen, S.C. Figueiredo, Z. Li, Z. Chang, K. Jansen, O. Çopuroğlu, E. Schlangen, Improving printability of limestone-calcined clay-based cementitious materials by using viscosity-modifying admixture, Cem. Concr. Res. 132 (2020), 106040, https://doi.org/10.1016/j.cemconres.2020.106040.

[13] N. Roussel, Rheological requirements for printable concretes, Cem. Concr. Res. 112 (2018) 76–85, https://doi.org/10.1016/j.cemconres.2018.04.005.

[14] N. Roussel, A thixotropy model for fresh fluid concretes: theory, validation and applications, Cem. Concr. Res. 36 (10) (2006) 1797–1806, https://doi.org/10.1016/j.cemconres.2006.05.025.

[15] R.A. Buswell, W.L. de Silva, S. Jones, J. Dirrenberger, 3D printing using concrete extrusion: a roadmap for research, Cem. Concr. Res. 112 (2018) 37–49, https://doi.org/10.1016/j.cemconres.2018.05.006.

[16] B. Panda, C. Unluer, M.J. Tan, Investigation of the rheology and strength of geopolymer mixtures for extrusion-based 3D printing, Cem. Concr. Compos. 94 (2018) 307–314, https://doi.org/10.1016/j.cemconcomp.2018.10.002.

[17] R. Comminal, W.R.L. da Silva, T.J. Andersen, H. Stang, J. Spangenberg, Modelling of 3D concrete printing based on computational fluid dynamics, Cem. Concr. Res. 138 (2020), 106256, https://doi.org/10.1016/j.cemconres.2020.106256.

[18] N. Roussel, G. Ovarlez, S. Garrault, C. Brumaud, The origins of thixotropy of fresh cement pastes, Cem. Concr. Res. 42 (1) (2012) 148–157, https://doi.org/10.1016/j.cemconres.2011.09.004.

[19] J. Kruger, S. Zeranka, G. van Zijl, 3D concrete printing: a lower bound analytical model for buildability performance quantification, Autom. Constr. 106 (2019), 102904, https://doi.org/10.1016/j.autcon.2019.102904.

[20] A.S.J. Suiker, Mechanical performance of wall structures in 3D printing processes: theory, design tools and experiments, Int. J. Mech. Sci. 137 (2018) 145–170, https://doi.org/10.1016/j.ijmecsci.2018.01.010.

[21] R. Wolfs, A. Suiker, Structural failure during extrusion-based 3D printing processes, Int. J. Adv. Manuf. Technol. 104 (1–4) (2019) 565–584, https://doi.org/10.1007/s00170-019-03844-6.

[22] A. Perrot, Y. Mélinge, P. Estellé, C. Lanos, Vibro-extrusion: a new forming process for cement-based materials, Adv. Cem. Res. 21 (3) (2009) 125–133, https://doi.org/10.1680/adcr.2008.00030.

[23] A. Perrot, D. Rangeard, A. Pierre, Structural built-up of cement-based materials used for 3D-printing extrusion techniques, Mater. Struct. 49 (4) (2016) 1213–1220, https://doi.org/10.1617/s11527-015-0571-0.

[24] B. Panda, S. Chandra Paul, M. Jen Tan, Anisotropic mechanical performance of 3D printed fiber reinforced sustainable construction material, Mater. Lett. 209 (2017) 146–149, https://doi.org/10.1016/j.matlet.2017.07.123.

[25] B. Panda, J.H. Lim, M.J. Tan, Mechanical properties and deformation behaviour of early age concrete in the context of digital construction, Compos. Part B 165 (2019) 563–571, https://doi.org/10.1016/j.compositesb.2019.02.040.

[26] S.C. Paul, Y.W.D. Tay, B. Panda, M.J. Tan, Fresh and hardened properties of 3D printable cementitious materials for building and construction, Arch. Civil Mech. Eng. 18 (1) (2018) 311–319, https://doi.org/10.1016/j.acme.2017.02.008.

[27] T. Wangler, E. Lloret, L. Reiter, N. Hack, F. Gramazio, M. Kohler, M. Bernhard, B. Dillenburger, J. Buchli, N. Roussel, Digital concrete: opportunities and challenges, RILEM Technical Lett. 1 (2016) 67–75, https://doi.org/10.21809/rilemtechlett.2016.16.

[28] J. Kruger, S. Cho, S. Zeranka, C. Viljoen, G. van Zijl, 3D concrete printer parameter optimisation for high rate digital construction avoiding plastic collapse, Compos. Part B 183 (2019), 107660, https://doi.org/10.1016/j.compositesb.2019.107660.

[29] T. Lecompte, A. Perrot, Non-linear modeling of yield stress increase due to SCC structural build-up at rest, Cem. Concr. Res. 92 (2017) 92–97, https://doi.org/10.1016/j.cemconres.2016.11.020.

[30] A. Perrot, A. Pierre, S. Vitaloni, V. Picandet, Prediction of lateral form pressure exerted by concrete at low casting rates, Mater. Struct. 48 (7) (2015) 2315–2322, https://doi.org/10.1617/s11527-014-0313-8.

[31] A.S. Suiker, R.J. Wolfs, S.M. Lucas, T.A. Salet, Elastic buckling and plastic collapse during 3D concrete printing, Cem. Concr. Res. 135 (2020), 106016, https://doi.org/10.1016/j.cemconres.2020.106016.

[32] R. Wolfs, F. Bos, T. Salet, Triaxial compression testing on early age concrete for numerical analysis of 3D concrete printing, Cem. Concr. Compos. 104 (2019), 103344, https://doi.org/10.1016/j.cemconcomp.2019.103344.

[33] T. Ooms, G. Vantyghem, R. Van Coile, W. De Corte, A parametric modelling strategy for the numerical simulation of 3D concrete printing with complex geometries, Addit. Manufact. 38 (2021), 101743, https://doi.org/10.1016/j.addma.2020.101743.

[34] R. Jayathilakage, P. Rajeev, J. Sanjayan, Yield stress criteria to assess the buildability of 3D concrete printing, Constr. Build. Mater. 240 (2020), 117989, https://doi.org/10.1016/j.conbuildmat.2019.117989.

[35] R. Wolfs, F. Bos, T. Salet, Early age mechanical behaviour of 3D printed concrete: numerical modelling and experimental testing, Cem. Concr. Res. 106 (2018) 103–116, https://doi.org/10.1016/j.cemconres.2018.02.001.

[36] G. Vantyghem, T. Ooms, W. De Corte, FEM modelling techniques for simulation of 3D concrete printing, arXiv preprint arXiv:.06907, 2020, https://doi.org/10.48550/arXiv.2009.06907.

[37] Z. Chang, Y. Xu, Y. Chen, Y. Gan, E. Schlangen, B. Šavija, A discrete lattice model for assessment of buildability performance of 3D-printed concrete, Comput. Aided Civil Infrastruct. Eng. 36 (5) (2021) 638–655, https://doi.org/10.1111/mice.12700.

[38] Z. Qian, Multiscale Modeling of Fracture Processes in Cementitious Materials, Delft University of Technology, 2012. http://resolver.tudelft.nl/uuid:734b276c-283a-4f7a-8db2-a184453e8dac.

[39] S. Berton, J.E. Bolander, Crack band model of fracture in irregular lattices, Comput. Methods Appl. Mech. Eng. 195 (52) (2006) 7172–7181, https://doi.org/10.1016/j.cma.2005.04.020.

[40] J.E. Bolander, N. Sukumar, Irregular lattice model for quasistatic crack propagation, Phys. Rev. B 71 (9) (2005), 094106, https://doi.org/10.1103/PhysRevB.71.094106.

[41] H. Zhang, B. Šavija, Y. Xu, E. Schlangen, Size effect on splitting strength of hardened cement paste: experimental and numerical study, Cem. Concr. Compos. 94 (2018) 264–276, https://doi.org/10.1016/j.cemconcomp.2018.09.018.

[42] H. Zhang, Y. Xu, Y. Gan, Z. Chang, E. Schlangen, B. Šavija, Microstructure informed micromechanical modelling of hydrated cement paste: techniques and challenges, Constr. Build. Mater. 251 (2020), 118983, https://doi.org/10.1016/j.conbuildmat.2020.118983.

[43] M. Yip, J. Mohle, J. Bolander, Automated modeling of three-dimensional structural components using irregular lattices, Comput. Aided Civil Infrastruct. Eng. 20 (6) (2005) 393–407, https://doi.org/10.1111/j.1467-8667.2005.00407.x.

[44] Z. Qian, E. Schlangen, G. Ye, K. van Breugel, Modeling framework for fracture in multiscale cement-based material structures, Materials (Basel) 10 (6) (2017), https://doi.org/10.3390/ma10060587.

[45] E. Schlangen, J.G.M. Van Mier, Simple lattice model for numerical simulation of fracture of concrete materials and structures, Mater. Struct. 25 (9) (1992) 534–542, https://doi.org/10.1007/BF02472449.

[46] H. Zhang, B. Šavija, S. Chaves Figueiredo, M. Lukovic, E. Schlangen, Microscale testing and modelling of cement paste as basis for multi-scale modelling, Materials (Basel) 9 (11) (2016), https://doi.org/10.3390/ma9110907.

[47] Z. Chang, H. Zhang, E. Schlangen, B. Šavija, Lattice fracture model for concrete fracture revisited: calibration and validation, Appl. Sci. 10 (14) (2020) 4822, https://doi.org/10.3390/app10144822.

[48] M. Gebler, A.J.M. Schoot Uiterkamp, C. Visser, A global sustainability perspective on 3D printing technologies, Energy Policy 74 (2014) 158–167, https://doi.org/10.1016/j.enpol.2014.08.033.

[49] N. Jiang, H. Zhang, Z. Chang, E. Schlangen, Z. Ge, B. Šavija, Discrete lattice fracture modelling of hydrated cement paste under uniaxial compression at micro-scale, Constr. Build. Mater. 263 (2020), 120153, https://doi.org/10.1016/j.conbuildmat.2020.120153.

[50] E. Schlangen, E.J. Garboczi, Fracture simulations of concrete using lattice models: computational aspects, Eng. Fract. Mech. 57 (2–3) (1997) 319–332, https://doi.org/10.1016/S0013-7944(97)00010-6.

[51] H. Zhang, Y. Xu, Y. Gan, Z. Chang, E. Schlangen, B.J.C. Šavija, C. Research, Combined experimental and numerical study of uniaxial compression failure of hardened cement paste at micrometre length scale, Cem. Concr. Res. 126 (2019), 105925, https://doi.org/10.1016/j.cemconres.2019.105925.

[52] C. Yu, P. Hoogenboom, J. Rots, Extension of incremental sequentially linear analysis to geometrical non-linearity with indirect displacement control, Eng. Struct. 229 (2021), 111562, https://doi.org/10.1016/j.engstruct.2020.111562.

[53] J.S. Przemieniecki, Matrix Structural Analysis, Courier Corporation, 1985. https://books.google.nl/books?hl=zh-CN&lr=&id=Pb8qTzqOKbAC&oi=fnd&pg=PA1&dq=Matrix+structural+analysis&ots=NQP_1Vi6-V&sig=34iip2vXWhWj2bYe-iG6dP5CRCE&redir_esc=y#v=onepage&q=Matrix%20structural%20analysis&f=false.

[54] R. De Borst, M.A. Crisfield, J.J. Remmers, C.V. Verhoosel, Nonlinear Finite Element Analysis of Solids and Structures, John Wiley & Sons, 2012. https://books.google.nl/books?hl=zh-CN&lr=&id=OxXRwNy-4gQC&oi=fnd&pg=PT9&dq=Nonlinear+finite+element+analysis+of+solids++694++and+structures&ots=mlFYNxzaj0&sig=pZpUSaxzBz7S0Pv_yC03xMJyUmY&redir_esc=y#v=onepage&q&f=false.

[55] J.-Y. Petit, K.H. Khayat, E. Wirquin, Coupled effect of time and temperature on variations of yield value of highly flowable mortar, Cem. Concr. Res. 36 (5) (2006) 832–841, https://doi.org/10.1016/j.cemconres.2005.11.001.
[56] Y. Gan, C. Romero Rodriguez, H. Zhang, E. Schlangen, K. van Breugel, B. Šavija, Modeling of microstructural effects on the creep of hardened cement paste using an experimentally informed lattice model, Computer-Aided Civil Infrastruct. Eng. 36 (5) (2021) 560–576, https://doi.org/10.1111/mice.12659.
[57] P. Gao, Y. Chen, H. Huang, Z. Qian, E. Schlangen, J. Wei, Q. Yu, Effect of relative humidity on drying-induced damage in concrete: a comparative study of digital image correlation and lattice modelling, Mater. Des. 196 (2020), 109128, https://doi.org/10.1016/j.matdes.2020.109128.